Journal of Petroleum Exploration and Production Technology (2023) 13:1135–1153
https://doi.org/10.1007/s13202-022-01605-y

ORIGINAL PAPER - PRODUCTION ENGINEERING

# Stress evolution and fracture propagation of infill well after production and injection of parent well in a tight oil reservoir

**Shanzhi Shi[1] · Can Shi[2] · Gang Tian[1] · Botao Lin[3] · Huiyong Yu[1] · Shiming Wei[2] · Zejia Wang[1]**

Received: 17 June 2022 / Accepted: 31 December 2022 / Published online: 6 January 2023


## Abstract

Stimulation of unconventional tight oil formations via horizontal wells has seen increasing cases of fracturing infill wells in recent years. The effectiveness of such a strategy is mainly dependent on the proper characterization of the stress evolution and an accurate forecast of the subsequent fracture propagation in the region neighboring the infill wells after considering the production performance and the injection schemes of the parent wells. In this respect, a comprehensive approach was proposed to simulate the stress evolution caused by the production and injection of the parent wells. The approach can also predict the upcoming fracture propagation behavior of the infill well. It was found that depletion in the parent wells can result in dramatic changes of the stress field, highlighted by apparent decreases in the magnitude of the minimum horizontal stress and changes in its orientation. Controlled injection in the parent wells can reproduce the original stress field, which favors the transverse extension of the fracture network in the infill well. In contrast, soaking well alone has little effect on improving the stress field. Therefore, this study suggests optimal injection schemes for parent wells and provides insights for fracture cluster designs in an infill well, eventually leading to maximized productivity of the infill well.

**Keywords** Tight oil formation · Conglomerate reservoir · Stress evolution · Injection · Infill well · Parent well

## List of symbols

| | |
|---|---|
| $C$ | The average conductivity of hydraulic fractures, D cm |
| $\boldsymbol{C}$ | The stiffness matrix, Pa |
| $c_m$ | The compressibility of the rock matrix, dimensionless |
| $E$ | The Young's modulus, Pa |
| $G$ | The shear modulus, Pa |
| $H$ | The height of the fracture, m |
| $\boldsymbol{I}$ | The unit diagonal matrix, dimensionless |
| $K$ | The drained volumetric modulus of the skeleton, Pa |
| $k_m$ | The rock matrix permeability, dimensionless |
| $L$ | The length of the fracture, m |
| $n_f$ | The unit normal vector of fracture surface, dimensionless |
| $\boldsymbol{n}_f^+$ and $\boldsymbol{n}_f^-$ | The unit norm vector of the two fractures surfaces, m |
| $p$ | The pore pressure, Pa |
| $p_0$ | The initial pore pressure, Pa |
| $p_w$ | The local fracture width, m |
| $Q$ | The fluid injection rate, $m^2/s$ |
| $Q_f$ | The mass transfer rate between the matrix and fractures, $kg/m^3/s$ |
| $Q_m$ | The mass source of the fluid flow in the rock matrix, $kg{\cdot}s^{-1}{\cdot}m^{-3}$ |
| $r$, $\varphi$ | The local polar coordinate system at fracture tips |
| $S$ | The strain energy, J |
| $T$ | Tensile strength, Pa |
| $\boldsymbol{u}_f^+$ and $\boldsymbol{u}_f^-$ | The displacements of the two fracture surfaces, m |
| $v$ | The Poisson's ratio, dimensionless |
| $V_\mathrm{d}$ | The depletion fluid volume, $m^3$ |
| $V_\mathrm{f}$ | The fracturing fluid volume, $m^3$ |
| $V_\mathrm{i}$ | The injection fluid volume, $m^3$ |
| $V_\mathrm{p}$ | The production fluid volume, $m^3$ |

✉ Can Shi
shican940111@163.com

[1] Engineering Technology Research Institute, PetroChina Xinjiang Oilfield Company, Karamay 834000, Xinjiang, China

[2] College of Petroleum Engineering, China University of Petroleum, Beijing 102249, China

[3] College of Artificial Intelligence, China University of Petroleum, Beijing 102249, China

| | |
|---|---|
| $w_0$ | The width of the fracture, m |
| $w_f$ | The fracture aperture, m |
| $\alpha$ | The Biot coefficient, dimensionless |
| $\Gamma^+f$ and $\Gamma^-f$ | The fracture surfaces |
| $\delta p$ | The test function, dimensionless |
| $\varepsilon$ | Strain, dimensionless |
| $\varepsilon_v$ | The volumetric strain of the rock matrix, dimensionless |
| $\mu_{\mathrm{f}}$ | Is the frac-fluid viscosity, mPa·s |
| $\xi_i$ | The injection coefficient, dimensionless |
| $\rho$ | The density of the rock matrix, kg·m$^{-3}$ |
| $\rho_{\mathrm{o}}$ | The density of the oil, kg·m$^{-3}$ |
| $\boldsymbol{\sigma}$ | Stress, Pa |
| $\sigma_0$ | The initial stress, Pa |
| $\sigma_{\mathrm{H0}}$ | The initial maximum horizontal stress, Pa |
| $\sigma_{\mathrm{h0}}$ | The initial minimum horizontal stress, Pa |
| $\sigma_{rr}$, $\sigma_{\varphi\varphi}$, and $\sigma_{r\varphi}$ | The stress indicators in the fracture coordinate, Pa |
| $\phi_m$ | The rock matrix porosity, dimensionless |
| $\chi_m$ | The total compressibility coefficient of the saturated rock matrix, Pa$^{-1}$ |

## Introduction

The infill well deployment has become increasingly popular in developing tight oil and gas reservoirs, answering a call for enhanced production of unconventional reserves such as some major shale, tight sandstone, and conglomerate plays (Zhang et al. 2011; Miller et al. 2016; Lindsay et al. 2018; Li et al. 2019; Shi et al. 2022). In this respect, the infill well fracture quality is crucial to achieving a controlled resource recovery ratio. The infill well fractures quality is described to be the degree to how transversely the hydraulic fractures grow relative to the horizontal wellbore and how extensive they would reach the controlled resource (Guo et al. 2019a). Besides the mechanical nature of the formation, it is strongly dependent on the stress evolution due to parent well production and specific measures taken on the parent wells, such as water injection.

The flow mode (production or injection), flow rate, original stress field, initial stress anisotropy, permeability anisotropy, pressure depletion, interwell interference, and preexisting fractures are believed to be the key factors affecting the stress reorientations and magnitude changes (Hidayati et al. 2001; Marongiu-Porcu et al. 2016; Guo et al. 2019a). Therefore, for a specific well pad with a prescribed well structure, existing natural or hydraulic fractures, and far-field structural stress field, the production history serves as the critical parameter that governs the evolution of the stress field in the pad, which leads to very heterogeneous maximum horizontal stress ($\sigma_H$) orientations around parent well fractures (Guo et al. 2019a). In industry, it has long been observed that when developing infill wells, the parent well production induce significant stress alteration in the well pad, generating interwell interference and affecting the hydraulic fracture path along with infill wells. The production further affects the completion quality and underperformance of the infill wells (Settari and Mourits 1998; Gai et al. 2003; Dean et al. 2006; Zoback 2010; Ajani and Kelkar 2012; Gupta et al. 2012; Lindsay et al. 2018; Guo et al. 2019b). Therefore, understanding the stress field of the well pad after legacy production is of vital importance for the parent wells' operational measures and the infill wells' completion designs.

Because the reinjection of the parent wells can partially restore the original stress field, it is attractive to recharge the parent wells by injecting a certain amount of water before fracturing the infill well. Gakhar et al. discovered that refracturing a multi-well pad in Eagle Ford shale consisting of one parent well and one infill well of 1524 m increased the oil production by 11% after the parent well was recharged by injecting 6868.8 m$^3$ of water (Gakhar et al. 2017). Guo et al. found from numerical results on Eagle Ford shale that an injection volume of at least 76.9% of the total depleted liquid volume during the legacy production was needed to avoid fracture hits if the infill well clusters are appropriately located (Guo et al. 2019b). The amount of injection needed for the well pad to retrieve its original stress state does not apply to parent wells in a tight oil formation with a different completion strategy. In the meantime, it is desired to inject the water amount that would cause little interference of the subsequently completely infill well with the existing wells (Ajani and Kelkar 2012).

The interwell interference brought by parent well production and reinjection, and the fracture interference, can significantly impact the fracture path and configuration of the infill wells. The severity of the impact depends on factors such as well spacing and the age of the parent well (Gupta et al. 2020a). Roussel et al. revealed that a reduction in horizontal stress contrast one year after the onset time of stress reversal favors the interaction of hydraulic fractures in the infill well having natural fractures and enhances the fracture network complexity (Roussel et al. 2013). Kurtoglu et al. declared that the fracture interference between parent and infill wells is driven by three factors: the areal variation of reservoir properties, the production-induced pressure depletion, and the distance between the parent and infill wells (Kurtoglu and Salman 2015). Gupta et al. and Safari et al. uncovered that the fractures in the parent wells serve as either attractors or diverters of the hydraulic fractures in the infill well, dependent on whether the former set of fractures is injected or produced (Gupta et al. 2012; Safari et al. 2017). Guo et al. investigated the effects of legacy

production, differential stress, perforation cluster location, and parent well fracture geometry on the interwell hydraulic fracture geometries based on data from the Eagle Ford shale. They discovered that differential stress, legacy production, and fracture geometry strongly affect the infill well fracture growth, whereas the perforation cluster location has insignificant effects (Guo et al. 2019a). Gupta et al. analyzed the production data of MFHWs in the Haynesville shale to predict cumulative production and diagnose the impacted wells by fracture hits, refracturing and other factors (Gupta et al. 2020b). Fiallos et al. investigate the well interference in the Eagle Ford shale reservoir using numerical models in the combination of an embedded discrete fracture model (Fiallos et al. 2019). Yang et al. developed a two-fracture model to simulate the bottom-hole pressure (BHP) response of the two-well system with frac hits among simple fractures during shut-in period (Yang et al. 2020). He et al. researched the mechanism and dominated factors behind interwell fracturing interference in multi-well pads and found that a minor pressure difference between the infill well and parent wells is preferred to prevent fracturing interference (He et al. 2020). Dave et al. (2022) revealed that conductivity damage reactions of parent well production (Dave et al. 2022). They indicated that a single set of conductivity damage parameters are sufficient to replicate the productivity degradation observed during two separate frac hits on the parent well (one year apart) and children wells.

The research mentioned above efforts either used coupled flow and geomechanics models to perform sensitivity analysis on key parameters affecting stress field evolution or applied fracture models to investigate fracture propagation along with infill wells. In these modeling attempts, the artificial fractures along the parent wells were assigned to have uniform half-lengths or shortened half-lengths when taking stress shadow effects within a cluster. Although these sensitivity analyses have brought insightful understandings of factors affecting stress evolution, interwell interference, and fracture interference, they provide little evidence on these kinds of behavior in a field case. Moreover, the objects of the previous studies primarily focused on some significant shale plays in North America, whereas little information has been revealed on tight oil formations elsewhere. In such a respect, this study aims to examine the alteration of the stress magnitudes and the maximum horizontal stress azimuth upon depletion and subsequent reinjection of two full-scale parent wells in a natural conglomerate formation. Based on the stress field and the formation rock properties, the study investigates the fracture propagation in a deployed infill well, given the preset designs of fracture clusters and fracturing parameters. The production performances of the two different well pads having both parent and infill wells are used as field examples to verify the studied wells' stress evolution and fracture propagation.

## Geological and engineering background

The M region of the Mabei oil field is in the Mahu sag of the Junggar Basin, Xinjiang, northwest China. The oil-bearing area of the region is 449.34 $km^2$, covering a reserve of original oil in place (OOIP) at $2.09 \times 10^8$ tons, among which $2.86 \times 10^7$ tons are recoverable (Li et al. 2021; Zou et al. 2018). Since 2015, the contractor has been implementing horizontal well drilling and densely cut volumetric fracturing in the region, attempting to evaluate the engineering design factors, such as well length, cluster spacing, and fracturing volume on the production capacity of a horizontal well. After a series of research efforts and field tests, the well length ranges from 1000 to 3056 m with a fracturing volume of 2.5 to $8.8 \times 10^4$ $m^3$, while the cluster spacing was optimized to be 30 to 40 m (Li et al. 2019; Xu et al. 2019). However, the deployed horizontal wells commonly experienced a fast decline (21.5 ~ 76.7% in one year) and a low predicted recovery ratio (9.5% on average). Therefore, the drilling and completion of infill wells became necessary if targeted enhanced productivity. Given this background, the M region was selected for a pioneer project of the infill well deployment.

The major oil play in the M region is the Triassic Baikouquan formation formed of the gray sandy conglomerate stratum. The conglomerate gravels comprise 57.1% of the formation weight, while most of them have diameters ranging from 0.5 to 2 cm, peaking at 10 cm. The rest of the rock material is sand grains (36.9%), non-crystalline matrix (4.3%), and cementing agents (1.3%). The conglomerate gravels develop from subcircular to subangular shapes. The grain contacts are point and line contact types, the latter being the majority. The formation is also randomly scattered with debris-type sandstone facies. The nonclay minerals are primarily quartz, contributing to 45.8% of the rock matrix. The second primary mineral is plagioclase, comprising 29.3% of the rock matrix. The clay content ranges from 2.3 to 10.0% of the total weight and mainly comprises illite, chlorite, and kaolinite. Three parallel-aligned parent wells marked M-P1, M-P2 and M-P3 are selected from the M region for the subsequent investigation. The configuration, fracturing design, and production history of the three wells are listed in Table 1.

## Field model setup

Microseismic monitoring has been frequently used to image hydraulic fracture morphology (Maxwell et al. 2010). Linear regression was the most common method for building the 2D planar fracture network, conveniently

**Table 1** Horizontal well configuration and fracturing parameters

| Well name | M-P1 | M-P2 | M-P3 |
|---|---|---|---|
| Depth (m) | 3270–4070 | 3273–3410 | 3275–3416 |
| Horizontal length (m) | 800 | 2005 | 2007 |
| Clusters in a single stage | 2 | 3 | 3 |
| Cluster distance (m) | 30–40 | 20–30 | 20–30 |
| Number of stages | 12 | 26 | 22 |
| Production date | 09/2013 | 12/2015 | 12/2015 |

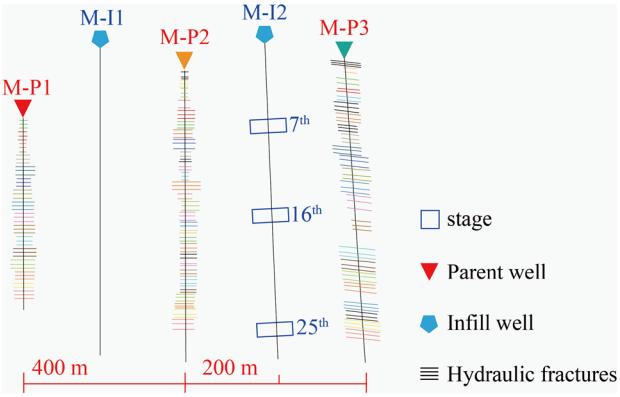


**Fig. 2** Geometric model for the studied well pad

characterizing natural and hydraulic fractures (Fisher et al. 2005). However, because of the existence of an unknown amount of noise (outliers) among the microseismic data, a direct fitting method might lead to results that are not reliable (Liu et al. 2018). In this regard, a robust occurrence calculation method based on the Random Sample Consensus (RANSAC) was applied to handle such a problem (Fisvhler and Bolles 1981, Liu et al. 2018). Figure 1 shows a field example that provides the morphology of hydraulic fractures interpreted by the integrated RANSAC method following Liu et al. (2018).

Figure 2 displays the 2D hydraulic fracture geometric models of wells M-P1, M-P2, M-P3, and M-I. M-P1, M-P2, and M-P3 are parent wells that have been producing for 5 to 7 years. The fractures of parent wells are generated by the integrated RANSAC method. The distance between the parent wells is 200 m on average. Well M-I2 is an infill well, located between wells M-P2 and M-P3. The fracture shape parameters can be imported to establish the geometric model for the subsequent numerical simulation. It must be clarified that the 2D numerical analysis on stress evolution and fracture propagation was adopted in this study when considering the well pad scale simulation. The 3D analysis is more legitimate but would give rise to a series of technical difficulties related to finite element analysis, computing power, and mechanisms inherent in fracture mechanics. These difficulties cannot be adequately handled for such a problem at the current stage. The formation properties used for the numerical simulation are listed in Table 2. The geomechanical and petrophysical properties were deduced from the laboratory tests, including the Kaiser stress experiments, triaxial tests, porosity measurements, permeability tests, chemistry analysis of crude oil, and fracture conductivity tests.

The research procedure consists of three steps, as shown in Fig. 3. First, the stress evolution caused by the production of the parent wells is investigated. Following this, the

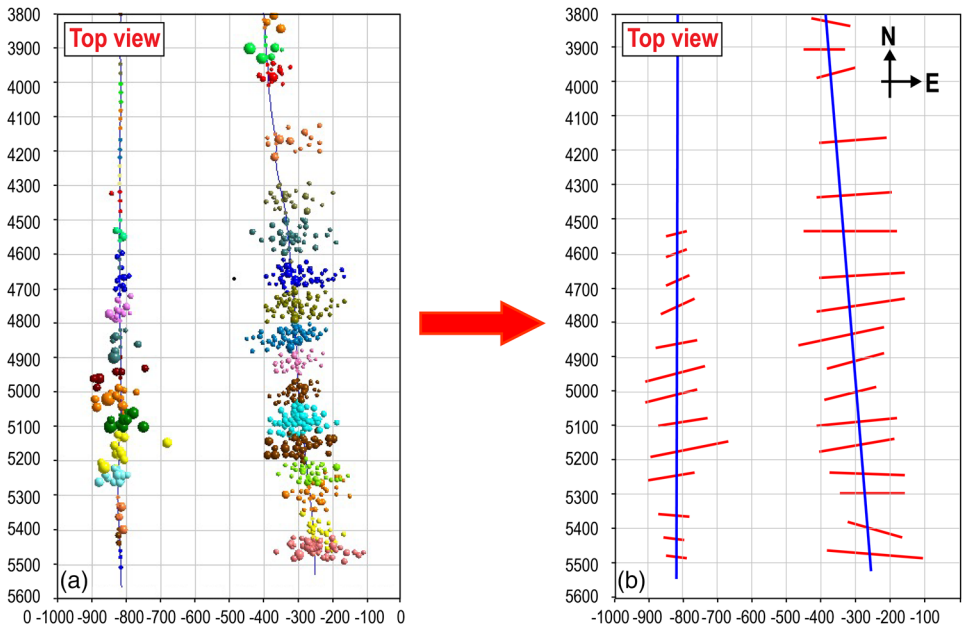


**Fig. 1** Hydraulic fractures generated by integrated RANSAC based on the microseismic events

**Table 2** Geological and engineering characteristics of the formation

| Parameter | Value |
|---|---|
| Depth $D$ (m) | 3092.8 |
| Oil density $\rho_o$ (g/cm$^3$) | 0.6445 |
| Oil viscosity $\mu_o$ (mPa·s) | 0.5 |
| Original formation pressure $p_0$ (MPa) | 55 |
| Original maximum horizontal stress $\sigma_{H0}$ (MPa) | 68 |
| Original minimum horizontal stress $\sigma_{H0}$ (MPa) | 68 |
| Orientation of $\sigma_{H0}$ (-) | NE85°~NE95° |
| Young's modulus $E$ (GPa) | 25.77 |
| Volumetric modulus $K$ (GPa) | 14.61 |
| Tensile strength $T$ (MPa) | 2.3 |
| Poisson's ratio $v$ (-) | 0.21 |
| Porosity of the matrix $\phi_m$ (%) | 7.63 |
| Permeability of the matrix $k_m$ (mD) | 1.33 |
| Viscosity of the fracturing fluid $\mu_f$ (mPa·s) | 27~36 |
| Average width of hydraulic fractures $w_f$ (mm) | 7.13 |
| Average conductivity of hydraulic fractures $C$ (D·cm) | 26.8 |

research compares the effects of reinjection and soaking at the two parent wells (M-P2 and M-P3) on stress evolution. Finally, the influences of the injection volume, soaking time, and wellhead pressure at the two parent wells on the fracture development of a perforation cluster in the infill well (M-I) are evaluated. Comparing the fracture propagation geometry of infill wells under different construction schemes of parent wells can help field engineers select a reasonable construction scheme for parent wells, such as reinjection or soaking, leading to maximized productivity of infill wells.

## Governing equations for stress evolution and fracture propagation

### Governing equations for the stress evolution

The constitutive relation for the saturated porous rock can be written as (Gao et al. 2020)

$$\boldsymbol{\sigma} = \boldsymbol{\sigma}_0 + \boldsymbol{C} : \boldsymbol{\varepsilon} - \alpha(p - p_0)\boldsymbol{I} \tag{1}$$

where $\boldsymbol{\sigma}$ and $\boldsymbol{\varepsilon}$ are the stress and strain, respectively; $\sigma_0$ represents the initial stress, Pa. $\boldsymbol{C}$ is the stiffness matrix, Pa; $\alpha$ is the Biot coefficient, dimensionless; $p$ is the pore pressure, Pa; $p_0$ is the initial pore pressure, Pa; $\boldsymbol{I}$ is the unit diagonal matrix, dimensionless. The rock strain tensor can be represented using the solid displacement expressed as

$$\boldsymbol{\varepsilon} = \frac{1}{2}\left(\nabla \boldsymbol{u} + \nabla^T \boldsymbol{u}\right) \tag{2}$$

where $\boldsymbol{u}$ is the displacement vector, m. The momentum conservation equation for the porous rock is

$$\nabla \cdot \boldsymbol{\sigma} + \rho \boldsymbol{g} = 0 \tag{3}$$

where $\rho$ is the density of the rock matrix, kg·m.$^{-3}$. The governing equation for flow is controlled by the pore pressure and can be written as (Wei et al. 2018)

$$\rho \chi_m \frac{\partial p}{\partial t} - \nabla \cdot (\rho \frac{k_m}{\mu} \nabla p) = Q_m \tag{4}$$

$$\chi_m = (1 - \phi_m) c_m + \phi_m c_w \tag{5}$$

where $\chi_m$ is the total compressibility coefficient of the saturated rock matrix, Pa$^{-1}$; $k_m$ is the rock matrix permeability; $\phi_m$ is the rock matrix porosity; $c_m$ is the compressibility of the rock matrix; $Q_m$ is the mass source of the fluid flow in the rock matrix, kg·s$^{-1}$·m.$^{-3}$. Considering the pseudo-steady deformation of the rock, the mass source of the fluid flow can be formulated as follows (Wei et al. 2021)

$$Q_m = -\alpha \rho \frac{\partial \varepsilon_v}{\partial t} = -\rho \frac{\alpha^2}{3K} \frac{\partial p}{\partial t} \tag{6}$$

where $\varepsilon_v$ is the volumetric strain of the rock matrix, dimensionless; $K$ is the drained volumetric modulus of the skeleton, Pa.

To simulate the production and injection of the parent well, as well as the fracture propagation in the child well, the equations below are applied (Wei et al. 2021):

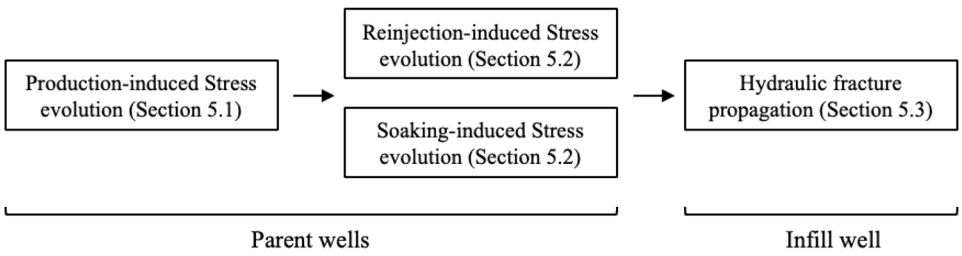


**Fig. 3** The flowchart of this research

$$\rho\chi_f\frac{\partial p}{\partial t}-\nabla\cdot(\rho\frac{w_f^2}{12\mu}\nabla p)=Q_f \tag{7}$$

$$Q_f=-\frac{k_m}{\mu}\nabla p\cdot\vec{n}_f \tag{8}$$

where $w_f$ is the fracture aperture, m. $n_f$ is the unit normal vector of the fracture surface. $Q_f$ is the mass transfer rate between the matrix and fractures, kg/m$^3$/s, which exists only on the fracture surfaces.

In the simulation, the original stress and pressure fields were used for the parent wells' initial stress and pressure states at the onset of their production, where the flow boundaries of the parent wells were set to have constant pressure. After production and reinjection of the parent wells, the stress and pressure fields were assigned as the initial state for the fracturing analysis of the infill well. During the simulation of the fracturing process in the infill well, zero flux condition was applied to the flow boundaries of the parent wells, while a constant flow rate was implemented on the boundary of the infill well.

## Governing equations for the fracture propagation

For an intact rock, once the hydraulic fracture initiates, each fracture node splits into two fracture nodes following an evaluation method of Wei et al. (2021), as illustrated in Fig. 4. The fracture aperture can therefore be expressed as

$$w_f=\left(\boldsymbol{u}_f^+\cdot\boldsymbol{n}_f^+ +\boldsymbol{u}_f^-\cdot\boldsymbol{n}_f^-\right) \tag{9}$$

where $\boldsymbol{u}_f^+$ and $\boldsymbol{u}_f^-$ are the displacements of the two fracture surfaces, m; $\boldsymbol{n}_f^+$ and $\boldsymbol{n}_f^-$ are the unit norm vector of the two fractures surfaces, m, respectively.

The minimum strain energy density method is adopted to judge the initiation of a fracture (Sih 1974)

$$\begin{cases}\left.\dfrac{\partial S}{\partial\varphi}\right|_{\varphi=\varphi_0}=0,\ \left.\dfrac{\partial^2 S}{\partial\varphi^2}\right|_{\varphi=\varphi_0}>0\\ S=\dfrac{1}{2\mu}\left[\dfrac{k_p+1}{8}\left(\sigma_{rr}+\sigma_{\varphi\varphi}\right)^2-\sigma_{rr}\sigma_{\varphi\varphi}+\sigma_{r\varphi}^2\right]\end{cases} \tag{10}$$

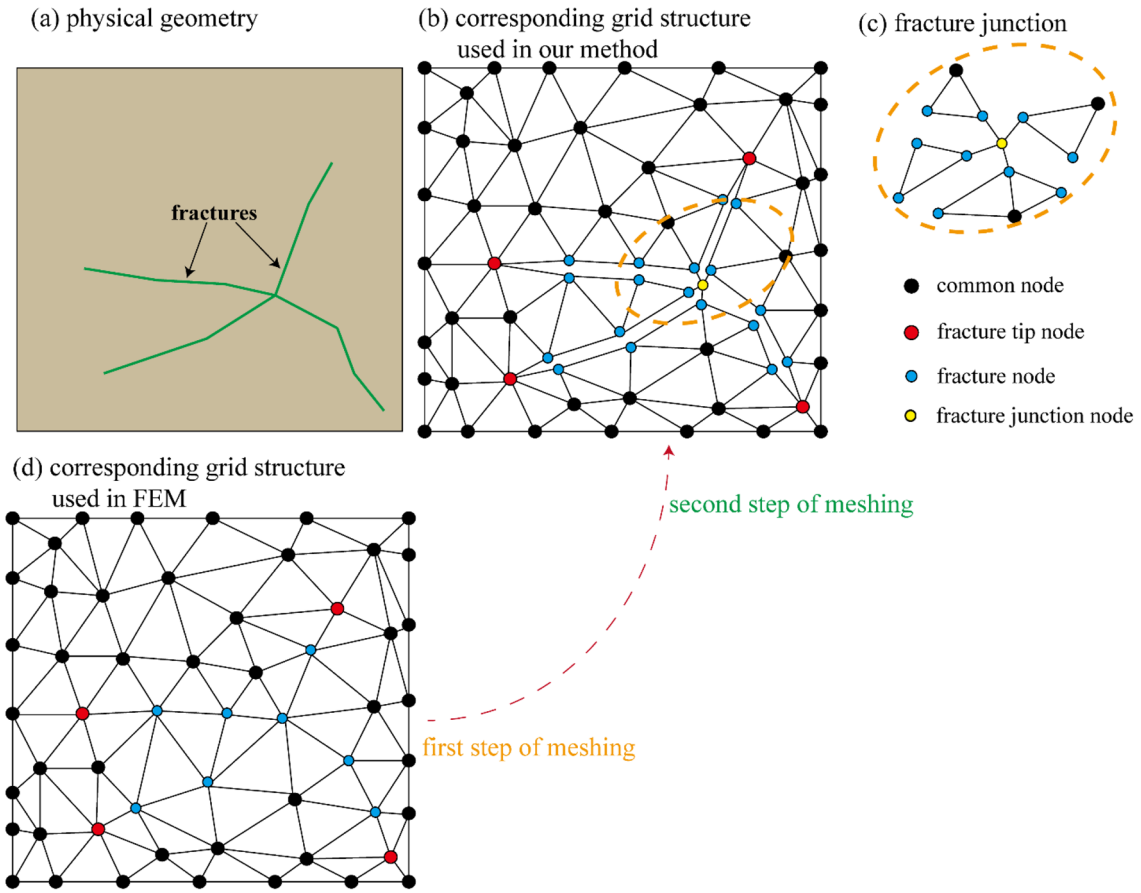


**Fig. 4** Two-dimensional illustration of the grid structure (Wei et al. 2021)

where $S$ is the strain energy, J; $(r, \varphi)$ is the local polar coordinate system at fracture tips; $\sigma_{rr}$, $\sigma_{\varphi\varphi}$, and $\sigma_{r\varphi}$ are the stress indicators in the fracture coordinate, Pa. The parameter $k_p$ varies under different circumstances:

$$k_p = \begin{cases} 3 - 4v \text{ (plane strain)} \\ \dfrac{3-v}{1+v} \text{ (plane stress)} \end{cases} \tag{11}$$

where $v$ is the drained Poisson's ratio of the saturated rock, dimensionless.

Equation (10) was used to judge whether a fracture in the infill well propagates; if so, the grid structure was modified following the procedure demonstrated in Fig. 3. At this moment, Eq. (9) was activated to evaluate the fracture aperture along the fracture path. Such a process recurs as soon as the aperture gets updated.

## Weak formulations

To obtain the variants needed in Sect. "Governing equations for the fracture propagation", finite element method (FEM) is employed to solve the mathematical model shown in Sect. "Governing equations for the stress evolution". The weak form of Eq. (4) is given below.

$$\begin{aligned} &\int_{\Omega_m} \left[\rho\left(\chi_m + \frac{\alpha^2}{3K}\right)\delta p \frac{\partial p}{\partial t} + \rho\frac{k_m}{\mu}\nabla\delta p \nabla p\right] d\Omega_m \\ &- \int_{\Gamma_f^{\pm}} \left(-\rho\frac{k_m}{\mu}\delta p \nabla p \cdot \boldsymbol{n}_f^{\pm}\right) d\partial\Omega_m \\ &- \int_{\Gamma_{mq}} \left[(\delta p \boldsymbol{q}_m)\cdot \boldsymbol{n}\right] d\partial\Omega_m = 0 \end{aligned} \tag{12}$$

where $\delta p$ is the test function. $\Gamma^+{}_f$ and $\Gamma^-{}_f$ represent the fracture surfaces.

The potential energy of a deformable saturated poroelastic media can be expressed as:

$$\begin{aligned} \pi_p = &\int_{\Omega_m} \frac{1}{2}\boldsymbol{\varepsilon}:\boldsymbol{\sigma} d\Omega - \int_{\Omega_m} \boldsymbol{u}\cdot\rho_s \boldsymbol{g} d\Omega - \int_{\Gamma_\sigma} \\ &\boldsymbol{u}\cdot\boldsymbol{T} d\Gamma - \int_{\Gamma_f^+} \boldsymbol{u}_f^+ \cdot \boldsymbol{T}_f^+ d\Gamma - \int_{\Gamma_f^-} \boldsymbol{u}_f^- \cdot \boldsymbol{T}_f^- d\Gamma \end{aligned} \tag{13}$$

After discretizing the variants with shape function $\boldsymbol{N}$, the variants at any position can be described using:

$$u = \boldsymbol{N}\boldsymbol{u}_e,\ p = \boldsymbol{N}\boldsymbol{p}_e \tag{14}$$

Substitute Eq. (14) into Eq. (13),

$$\pi_p = \sum \boldsymbol{u}_e^T \left\{ \begin{aligned} &\frac{1}{2}\int_{\Omega_m} (\mathbf{B}^T\mathbf{D}\mathbf{B}) d\Omega \boldsymbol{u}_e - \frac{1}{2}\int_{\Omega_m} (\alpha \mathbf{B}^T \boldsymbol{N}) d\Omega \boldsymbol{p}_e - \int_{\Omega_m} (\boldsymbol{N}^T \rho_s \boldsymbol{g}) d\Omega \\ &- \int_{\Gamma_\sigma} \boldsymbol{N}^T \boldsymbol{T} d\Gamma - \int_{\Gamma_f^+} \boldsymbol{N}_f^T \boldsymbol{T}_f^+ d\Gamma - \int_{\Gamma_f^-} \boldsymbol{N}_f^T \boldsymbol{T}_f^- d\Gamma \end{aligned} \right\} \tag{15}$$

where

$$\mathbf{L} = \begin{bmatrix} \frac{\partial}{\partial x} & 0 \\ 0 & \frac{\partial}{\partial y} \\ \frac{\partial}{\partial y} & \frac{\partial}{\partial x} \end{bmatrix}, \mathbf{B} = \mathbf{L}\boldsymbol{N}$$

By deriving Eq. (15), the numerical equation of solid deformation used in FEM is obtained.

$$\mathbf{K}_u \boldsymbol{u} + \tilde{\mathbf{K}}_p \boldsymbol{p} = \boldsymbol{F}_u \tag{16}$$

$$\mathbf{K}_u = \frac{1}{2}\int_{\Omega_m} (\mathbf{B}^T\mathbf{D}\mathbf{B}) d\Omega \tag{17}$$

$$\tilde{\mathbf{K}}_p = \frac{1}{2}\int_{\Omega_m} (\alpha \mathbf{B}^T \boldsymbol{N}) d\Omega \tag{18}$$

$$\boldsymbol{F}_u = \int_{\Omega_m} (\boldsymbol{N}^T \rho_s \boldsymbol{g}) d\Omega + \int_{\Gamma_\sigma} \boldsymbol{N}^T \boldsymbol{T} d\Gamma + \int_{\Gamma_f^+} \boldsymbol{N}_f^T \boldsymbol{T}_f^+ d\Gamma + \int_{\Gamma_f^-} \boldsymbol{N}_f^T \boldsymbol{T}_f^- d\Gamma \tag{19}$$

Substitute Eq. (14) into Eq. (12), the numerical equation of fluid flow used in FEM is obtained.

$$\mathbf{M}_p \frac{\partial \boldsymbol{p}}{\partial t} + \mathbf{K}_p \boldsymbol{p} = \boldsymbol{F}_p \tag{20}$$

$$\mathbf{M}_p = \int_{\Omega_m} \left[\rho\left(\chi_m + \frac{\alpha^2}{3K}\right)\boldsymbol{N}^T\boldsymbol{N}\right] d\Omega_m \tag{21}$$

$$\mathbf{K}_p = \int_{\Omega_m} \left(\rho\frac{k_m}{\mu}\nabla\boldsymbol{N}^T\nabla\boldsymbol{N}\right) d\Omega_m \tag{22}$$

$$\boldsymbol{F}_p = \int_{\Gamma_{mq}} \left[(\boldsymbol{N}^T\boldsymbol{q}_m)\cdot\boldsymbol{n}\right] d\partial\Omega_m \tag{23}$$

Equations (16) and (20) consist of the numerical equations used in the simulation process, i.e., Eq. (24).

$$\begin{bmatrix} \mathbf{M}_p & \mathbf{0} \\ \mathbf{0} & \mathbf{0} \end{bmatrix} \frac{\partial}{\partial t}\begin{pmatrix} \boldsymbol{p} \\ \boldsymbol{u} \end{pmatrix} + \begin{bmatrix} \mathbf{K}_p & \mathbf{0} \\ \tilde{\mathbf{K}}_p & \mathbf{K}_u \end{bmatrix}\begin{pmatrix} \boldsymbol{p} \\ \boldsymbol{u} \end{pmatrix} = \begin{pmatrix} \boldsymbol{F}_p \\ \boldsymbol{F}_u \end{pmatrix} \tag{24}$$

## Model validation

The poro-elasticity solution has been validated in our previous paper (Wei et al. 2021). The reliability and accuracy of fracture propagation model are validated through modeling the hydraulic fracture initiation and propagation. Figure 5 shows the comparison of the fracture geometry using the finite element (FE) model of this study and using the analytical solution by Geertsma and de Klerk (Geertsma and Klerk 1969). The analytical solution is developed for a plane strain, vertical, fluid-driven fracture propagating in a homogeneous, impermeable formation. Geertsma and de Klerk obtain the following approximate solutions (without fluid leak-off):

$$L = 0.68\left[\frac{GQ^3}{(1-v)\mu h^4}\right]^{\frac{1}{5}} t^{\frac{4}{5}} \tag{25}$$

$$w_0 = 2.5\left[\frac{(1-v)\mu Q^2}{Gh}\right]^{\frac{1}{5}} t^{\frac{1}{5}} \tag{26}$$

$$p_w = 0.96\left[\frac{2G^3 Q\mu}{(1-v)^3 L^6}\right]^{\frac{1}{4}} \tag{27}$$

where $G$ is the shear modulus, Pa; $Q$ is the fluid injection rate, m2/s; $v$ is the Poisson's ratio; $\mu$ is the frac-fluid viscosity; $h$ is the height of the fracture, m; $w_0$ is the width of the fracture; $p_w$ is the local fracture width; $L$ is the length of the fracture.

Table 3 shows the parameters of both models. The simulation results in Fig. 5 demonstrate that these two models match closely with each other.

## Simulation results and discussion

### Stress evolution before reinjection

There were two phases of oil production in the neighboring wells. In the first phase, the side well M-P1 produced 821 days starting from Sep 2013, yielding 11,156.79 t of produced crude oil. In the second phase starting from Dec 2015, the parent wells M-P2, and M-P3 yielded 23,686.88 and 26,170.95 t, respectively, while the side well M-P1 produced another 12,358.92 t of oil. The production history is given in Table 4.

The governing equations in Sect. "Governing equations for stress evolution and fracture propagation" were applied to the model in Sect. "Field model setup", based on which the problem was solved on the COMSOL finite element platform. The borehole pressure used for the production simulation and the pressure distribution of the simulation model are consistent with the field production log data. The production data obtained from the numerical simulation are close to the recorded, as displayed in Table 4. The formation pressure, minimum horizontal stress, and orientation of maximum

**Table 3** Input parameters for the model validation

| Parameters | Value |
|---|---|
| Formation pore pressure, *Pp* (MPa) | 0 |
| Injection rate, $Q$ ($m^2$/s) | 0.001 |
| Poisson's ratio, $\mu$ (-) | 0.20 |
| Young's modulus, E (GPa) | 40 |
| Fracture height, h (m) | 10 |
| Fracturing fluid viscosity, $v$ (Pa·s) | 0.5 |
| Maximum Horizontal Stress, $S_H$ (MPa) | 15 |
| Minimum Horizontal Stress, $S_h$ (MPa) | 10 |

$S_H$ and *Pp* are used for the calculation of the numerical model

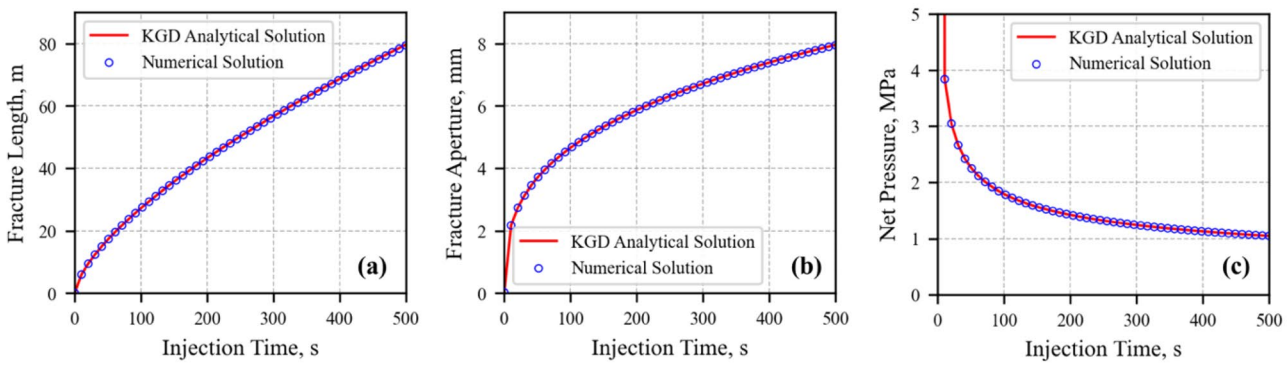


**Fig. 5** Simulated fracture geometry during different injection time spans using the KGD model and the model of this study: **a** fracture length; **b** fracture aperture; **c** net pressure

**Table 4** The production history of the side well and the two parent wells

| Phase # | Well # | Duration (days) | Overall field production (ton) | Average field production rate (ton/day) | Overall simulated production (ton) | Average simulated production rate (ton/day) |
|---|---|---|---|---|---|---|
| 1 | M-P1 | 821 | 11,156.79 | 13.59 | 10,903.5 | 13.28 |
| 2 | M-P1 | 1461 | 12,358.92 | 8.46 | 12,011 | 8.22 |
| | M-P2 | 1461 | 23,686.88 | 16.21 | 21,835.6 | 14.95 |
| | M-P3 | 1461 | 26,170.95 | 17.91 | 25,983 | 17.78 |

horizontal stress after phase one are calculated and presented in Fig. 6. It is demonstrated that after phase one production, the formation pressure $p$ in well M-P1 decreased from 35 to 12 MPa, while the minimum horizontal stress $\sigma_h$ declined from 56 to 46 MPa. The orientation of maximum horizontal stress $\sigma_H$ is most significantly affected at the south end of well M-P1, displaying a rotation of up to 30° to its original azimuth (marked by the red ellipse in Fig. 6c).

After phase two production, the formation pressure and minimum horizontal stress experience a further decrease, as demonstrated in Fig. 7. The minimum magnitude of $p$ and $\sigma_h$ exist in well M-P3, displaying a value of 10 and 40 MPa, respectively. Compare Fig. 7a and b, the influence of production on $\sigma_h$ is larger, and the $\sigma_h$ reduction area is mainly concentrated in the area parallel to the wellbore (red dotted box area). The orientation of $\sigma_H$ has been dramatically altered relative to its state after phase one production. The rotation angles can up to 50° at the end of the wellbore (with the most disturbed regions highlighted by blue circles). It must be noted that an upcoming infill (child) well (named well M-I2) is to be placed in between wells M-P2 and M-P3. Figure 8 shows the orientation of maximum horizontal stress along the M-I2 wellbore at different production time periods. The orientation angle of $\sigma_h$ significantly increases relative to the horizontal as the production time increases. Therefore, the depleted pressure and the changed azimuth of $\sigma_H$ can adversely influence the fracture network configuration and the corresponding SRV of the infill well.

The next step is to design a proper reinjection scheme that can restore to the maximum extent the original pressure, magnitudes, and orientations of the stresses. Meanwhile, the duration of soaking after injection would also play an important role in retrieving the initial pressure and stress states. A designed setup of injection schemes is given in Table 5. To quantitatively describe the total volume of injection fluid, an injection coefficient ($\xi_i$) is defined as the ratio of injection volume ($V_i$) to the depletion volume ($V_d$), being expressed as $\xi_i = V_i/V_d$. For example, if the depletion volume of M-P1 is 44655 $m^3$, and the total injection volume is 15111, then $\xi_i = 0.34$.

Schemes 1, 2, and 3 are compared to understand the effect of injection volume on the pressure and stress evolution as well as the fracture path in the infill well. Afterward, the cases of non-soaking after injection, soaking for 30 days after injection, and soaking for 100 days without injection, are compared to assess the effects of soaking on the pressure and stress (c.f., schemes 1, 4, and 5).

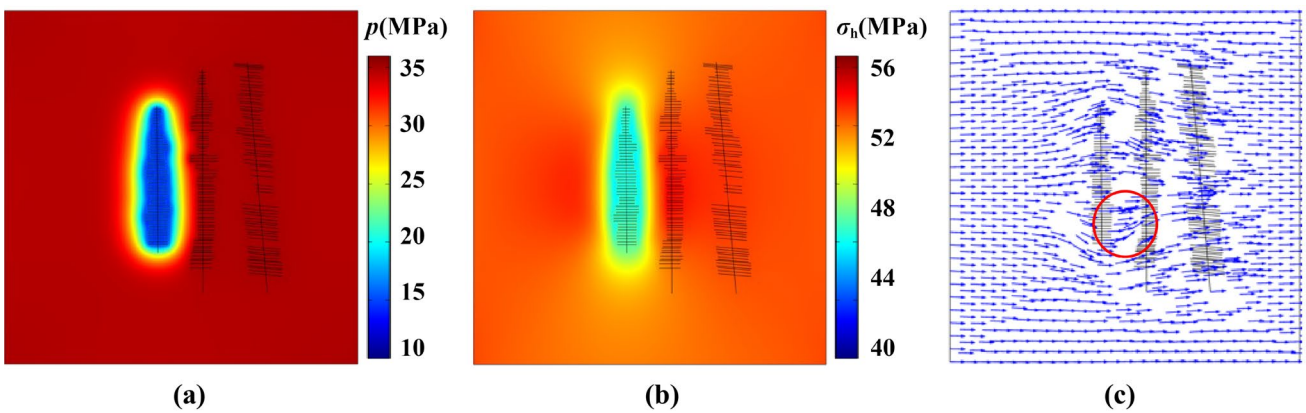


**Fig. 6** Pressure and stress fields after the phase one production: **a** formation pressure $p$; **b** minimum horizontal stress; **c** orientation of maximum horizontal stress $\sigma_H$

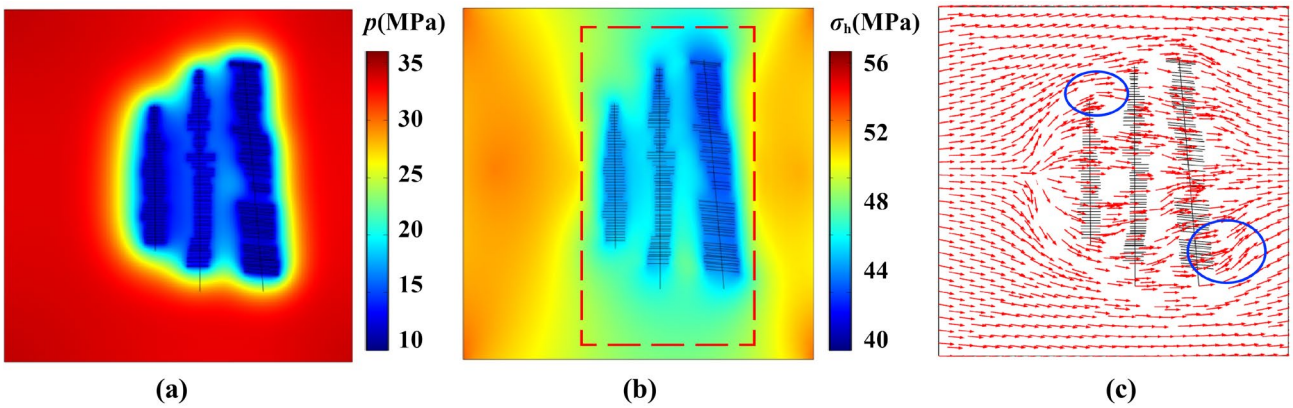


**Fig. 7** Pressure and stress fields after the phase two production: **a** formation pressure $p$; **b** minimum horizontal stress $\sigma_h$; **c** orientation of maximum horizontal stress $\sigma_H$

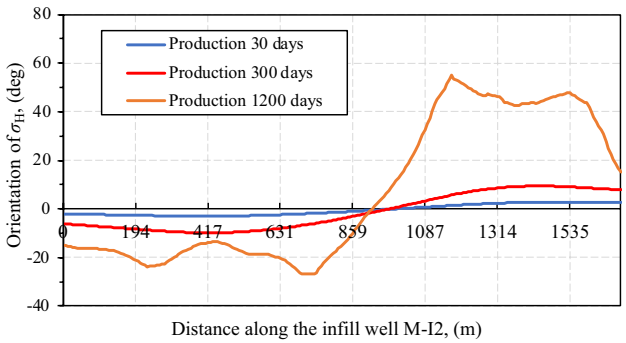


**Fig. 8** Orientation of maximum horizontal stress along the M-I2 wellbore at different production time spans

**Table 5** Different injection and soaking schemes for the parent well

| Schemes | 1 | 2 | 3 | 4 | 5 |
|---|---|---|---|---|---|
| $\xi_i$ (−) | 0 | 0.3 | 0.5 | 0.5 | 0.5 |
| Soaking time (d) | 0 | 0 | 0 | 30 | 100 |
| Figures | Fig. 7 | Fig. 9 | Fig. 10 | Fig. 12 | Fig. 13 |

## Effects of injection on pressure and stress field

It is discovered that the M-P1 production has little impact on the region between the M-P2 and M-P3 wells (c.f., Fig. 6). The effects of injection on pore pressure and stress field are evaluated in terms of the magnitude of pressure and the orientation of $\sigma_H$ (represented as blue-colored arrow lines in Fig. 9c), the latter of which largely determines the paths of the hydraulic fractures. Figure 9 represents the pressure and stress field after injection of the two parent wells M-P2 and M-P3 when $\xi_i = 0.3$, and Fig. 10 is the situation when $\xi_i = 0.5$.

Comparison of Fig. 7 and 9 indicates that through injection fluid into parent wells, the $\sigma_H$ azimuth turns further back to its original state. Meanwhile, the pressure increases accordingly in the fractured zone. It is worth notifying that the pressure in the fractured zone is greater than the far-field pressure (Fig. 9). Figure 11 shows the maximum horizontal stress orientation along the M-I2 wellbore at different injection volumes. At the 1200th day of production, the orientation of $\sigma_H$ near the M-I2 wellbore deflected significantly, with a maximum angle at approximately 60 degrees. However, the angle decreases with an increase in injection volume. When $\xi_i$ is equal to 0.5, the deflection angle becomes lower than 10 degrees. Consequently, the hydraulic fractures in an infill well between M-P2 and M-P3 will dilate along preferential planes of weakness and extend into the depleted zone of the parent wells, which can be detrimental to the two offset wells (Kurtoglu and Salman 2015). In contrast, the raised pressure in the fractured zone after injection can constrain the hydraulic fractures of the infill well within the light blue area at the right part of Fig. 11b, thereby decreasing the chances of harmful fracture interference. If a child well is deployed along the outer side of M-P2 or M-P3, then asymmetric fractures with a premier wing extending to the depleted area will develop along with the child well, deteriorating the productivity of the producer and the child well. The findings accord with Mukherjee et al. (1995) and Kurtoglu and Salman 2015.

The pressure in the fractured zone and the orientation are further compared between the case of soaking for 100 days (scheme 4 in Table 5) and the case of 100 days of soaking (scheme 5 in Table 5). A supplemental soaking duration is added to the injection to allow more time for the pressure in the fractured zone to dissipate to the unfractured zone. Again, the soaking alone exerts negligible impact on the pressure in the fractured zone, as shown in Figs. 12 and 13. On the other hand, soaking alone exerts little impact

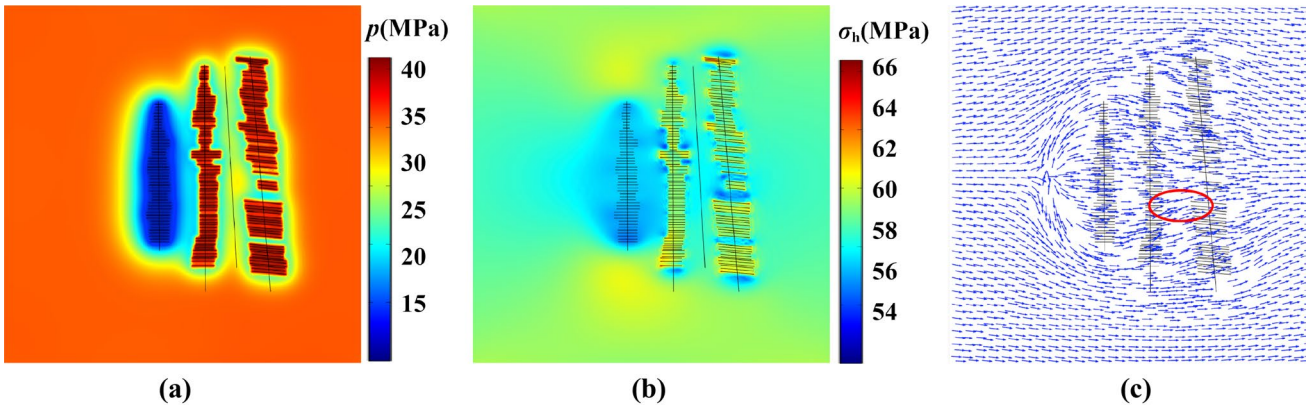


**Fig. 9** Pressure and stress field after injection of the two parent wells M-P2 and M-P3 when $\xi_i = 0.3$: **a** formation pressure $p$; **b** minimum horizontal stress; **c** orientation of maximum horizontal stress $\sigma_H$

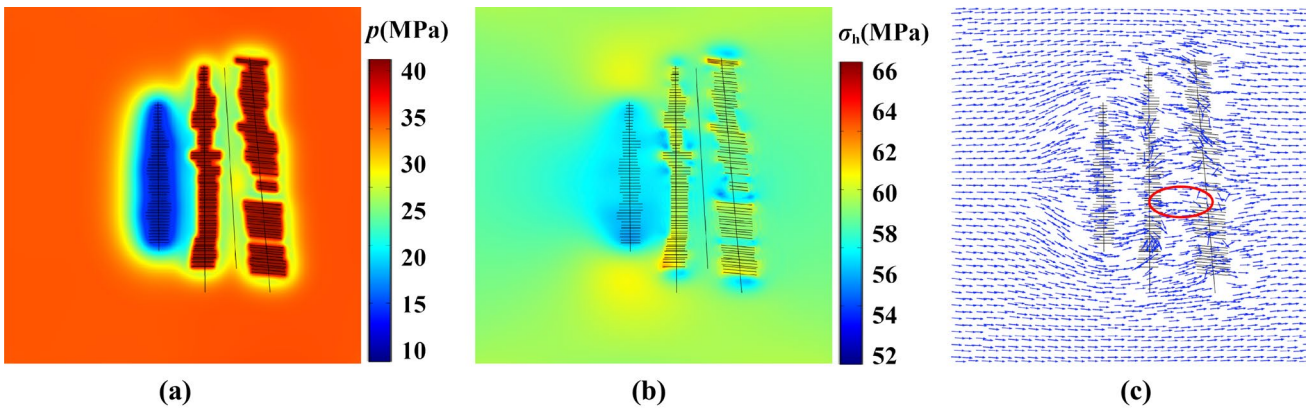


**Fig.10** Pressure and stress field after injection of the two parent wells M-P2 and M-P3 when $\xi_i = 0.5$: **a** formation pressure $p$; **b** minimum horizontal stress; **c** orientation of maximum horizontal stress $\sigma_H$

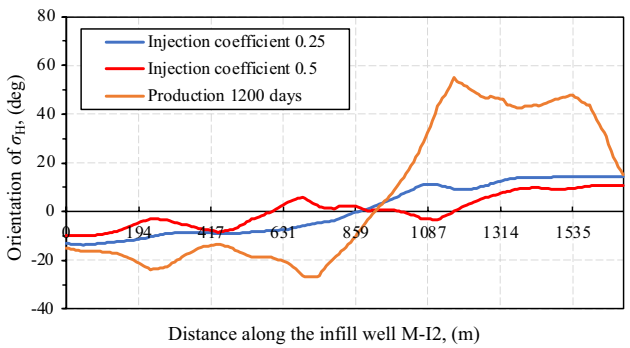


**Fig.11** The orientation of maximum horizontal stress along the M-I2 wellbore at different injection volumes

on either pressure or stress orientation, and such an impact is insensitive to the time spent in soaking (c.f., Figs. 12 and 13). Figure 14 shows the $\sigma_H$ orientation angles along the M-I2 wellbore at different injection volumes. Little difference exists in between these two cases with respect to the angle. In other words, soaking does not help restore the pressure and stress fields in the fractured zone neighboring the parent wells.

To further compare the effects of injection and soaking alone on the geomechanical responses neighboring the parent wells, the wellbore pressure magnitudes at one single well (M-P2) contributed by the two different mechanisms are presented in Fig. 15. It can be observed in Fig. 13 that soaking the well for 100 days has merely increased the wellbore pressure up to a level if an injection practice is implemented for merely three days.

The injection process retrieves the original stress orientation, which occurs most significantly at the middle zone of the two producers. The injection in the parent wells effectively retrieves the initial stress azimuth. As commonly recognized, the orientation of the maximum horizontal stress has crucial influences on the extension of transverse hydraulic fractures.

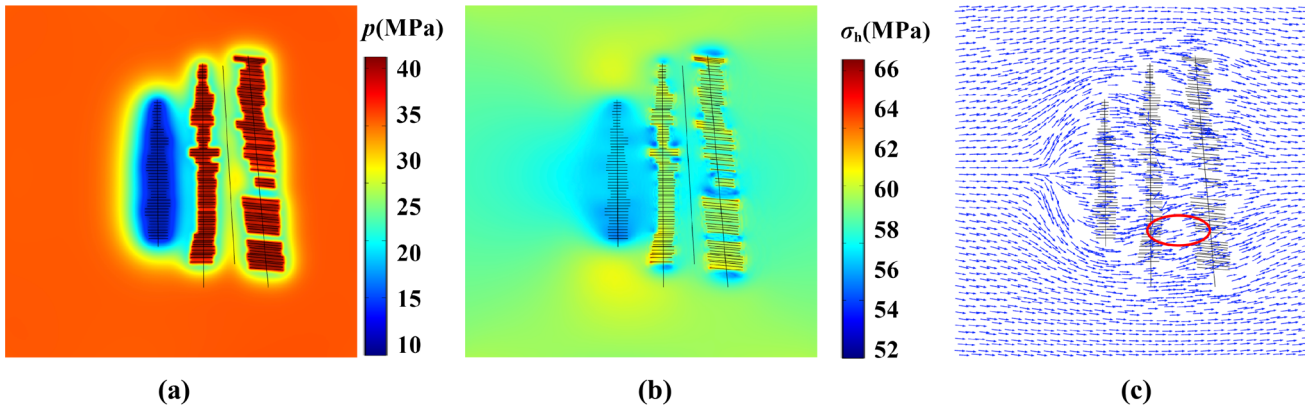


**Fig. 12** Pressure and stress field ($\xi_i$=0.5, soaking for 30 days): **a** formation pressure $p$; **b** minimum horizontal stress; **c** orientation of maximum horizontal stress $\sigma_H$

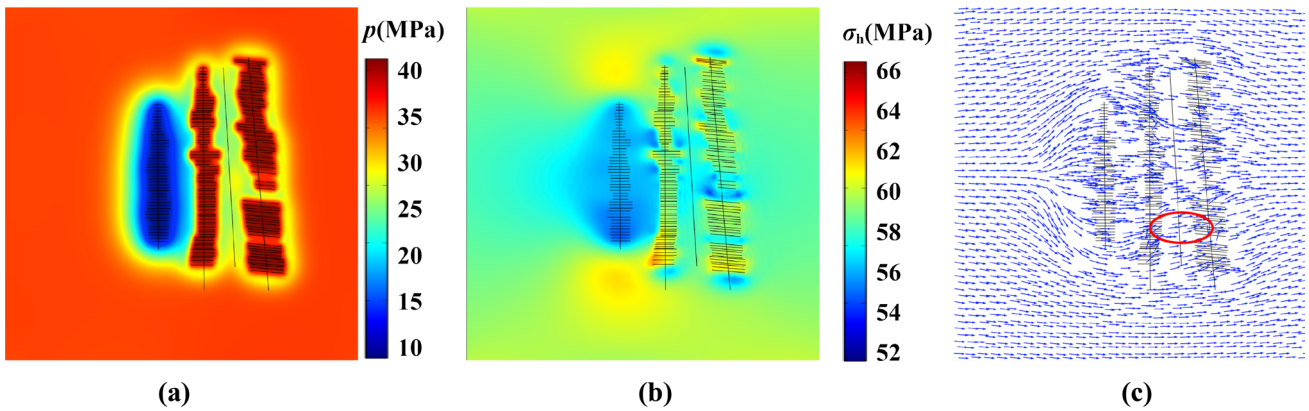


**Fig. 13** Pressure and stress field ($\xi_i$=0.5, soaking for 100 days): **a** formation pressure $p$; **b** minimum horizontal stress; **c** orientation of maximum horizontal stress $\sigma_H$

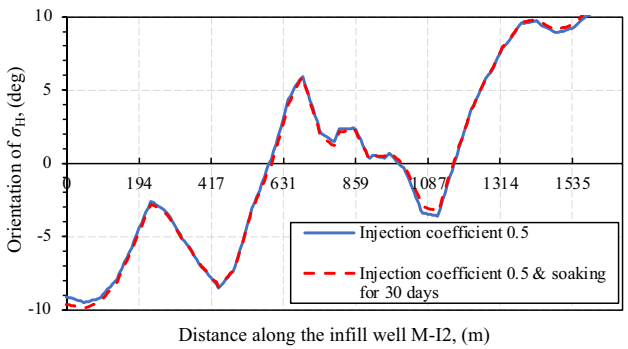


**Fig.14** Orientation angle of maximum horizontal stress along the M-I2 wellbore at different soaking time spans

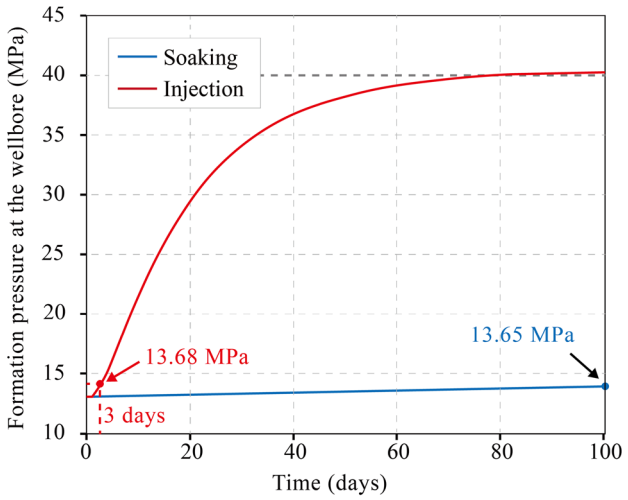


**Fig.15** Comparison between the influences of injection and of soaking on the wellbore pressure

## Effects of injection on fracture propagation in the infill well

The change in the effective stress field in an offset well can

bring either negative or positive fracture interference to the surrounding wells. Negative fracture interference occurs when the fractures of the offset well extend preferentially to the depleted zone of the neighboring producers and even connect with the fracture network of the latter. Such a scenario would lead to the production loss of the existing producers and sometimes the offset well (Kurtoglu and Salman 2015, Esquivel and Blasingame 2017). On the other hand, a proper design on the producer injection and the distance of the offset well deployment relative to the producers can result in positive interference where the fractures in the offset well extend without connection to the fracture network of the producers, giving rise to only recharge of the reservoir energy (Kurtoglu and Salman 2015, Guo et al. 2019a, b). In this respect, the influences of the injection volume, soaking time at the two parent wells (M-P2 and M-P3) on the fracture development of a perforation cluster in the infill well (M-I2) should be evaluated. Besides, the infill well is to be placed at the middle of the two parent wells, the influences of the distance between parent well and infill well on fracture propagation are evaluated on different sections of the infill well instead, which are at varying distances to the edges of the fractured zone of the parent wells. Figure 2 shows the positions of the stages as mentioned above. Table 6 is the different hydraulic fracturing schemes for the infill well, each scheme has different injection volume and soaking time.

**Table 6** Different hydraulic fracturing schemes for the infill well

| Schemes | 1 | 2 | 3 | 4 | 5 |
|---|---|---|---|---|---|
| $\xi_i$ (−) | 0 | 0.25 | 0.3 | 0.3 | 0.5 |
| Soaking (days) | 0 | 0 | 0 | 30 | 0 |
| Figures | 16(b) | 17(a) | 18(a) | 18(b) | 17(b) |

Well M-I2 reaches 3470 m in depth with a horizontal section of 2347 m. The wellhead of well M-I2 is located 204 m northwest to M-P3 and 221 m northwest to M-P2. M-I2 have 25 sections at an average length of about 90 m. Section 16 of the M-I2 well is selected for the fracturing simulation. The simulation design follows a consistent procedure among implementations of different injection volumes and soaking time spans. The fracturing fluid with a viscosity of 4 mPa·s is injected at an injection rate of 8 $m^3$/min. The simulation results for the different situations are presented in Figs. 10 and 11, respectively.

Figure 7c shows that the depletion of the parent wells causes a rotation of the fractures (relative to the normal direction) in the infill well ranging from 25 to 45 degrees due to the alteration of the stress field. Figure 16 shows the fracture geometry obtained by fracturing the infill wells directly after the production of the three old wells ended. Figure 16a shows the fracture propagation of the three clusters at the 16th stage, while Fig. 16b shows an enlarged view. The relatively small simulation time leads to the slightly extended fractures in the child well. As the legacy production time for parent wells increases, the fractures along the infill well become more longitudinal (Guo et al. 2019a, b). On the other hand, the complete fracturing process was not fully simulated given the limited computation time and difficult convergence of the model. It must be noted that a fracture is preferred if its configuration is perpendicular to the well and has less tortuosity; not only because a larger SRV can be achieved, but also the proppants can be more easily transported to the fracture tip. Therefore, the deflection of infill well fractures in this research demonstrates the quality of infill well completion, especially the SRV of the infill area.

Figure 16 shows that the fracture geometries at the infill well are complex, implying that the stress field has seriously been disturbed by the production of the parent wells.

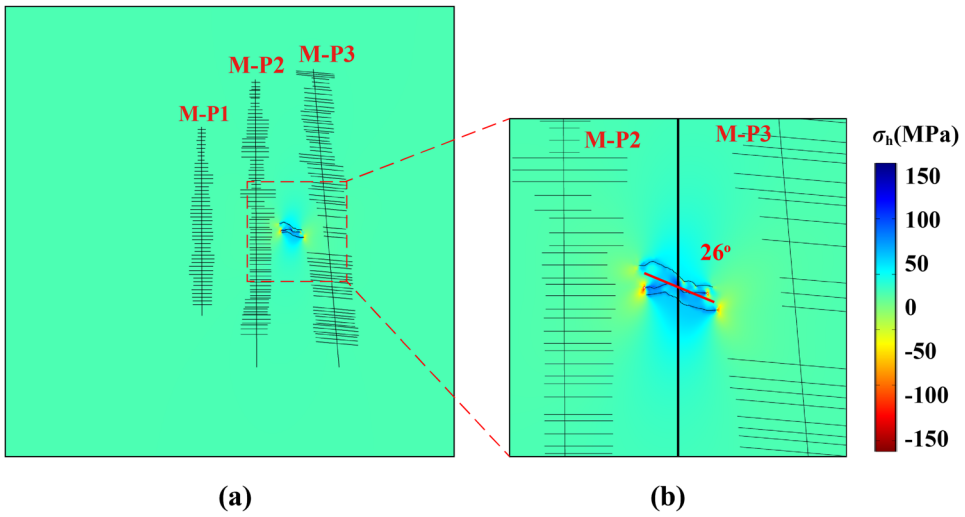


**Fig.16** The fracture configuration of the 16th stage of M-I2 after parent well production

The fracture extension of the infill well no longer develops perpendicular to the wellbore but tends toward the initial $\sigma_H$ direction. In such a scenario, additional stresses have been induced by hydraulic fractures (Li et al. 2010). The stresses are negative (tensile stress) near the fracture tips and become positive (compressive stresses) close to the middle segment of the fracture. Therefore, the stresses near the crack tip can be tensile and are much lower than in other zones.

Figure 17 displays the fracture propagation after fracturing the M-I2 using different injection volumes at the parent wells. As the $\xi_i$ increases from 0 to 0.25, 0.3, and 0.5, the rotation angle of the middle fracture (marked by the red line segment) decreases from 26 to 18, 16, and 2 degrees gradually (Figs. 16 and 17). The angle decreases with the increase in injection volume at the old well, and eventually reaches 2 degrees when $\xi_i$ becomes 0.5. In addition, a larger fracture deflection seems to be accompanied by stronger fracture interference. The two clusters of fractures in Fig. 16b repulse each other, whereas such an interference declines at an increased injection volume in the parent well.

Figure 18 examines the fracture patterns of the infill well under the zero and 30 days of soaking. Before soaking, both models are injected 0.3 times the depletion volume fluid to recover the formation pressure (schemes 3 & 4 in Table 6). The results show that the fracture deflection angle was reduced from 16 to 15 degrees after 30 days of soaking, indicating that soaking can only slightly improve the well interference. Either increasing the soaking time or raising the injection pressure can further reduce the angle of fracture rotation, with the latter measure having a much larger effect than the former. In other words, the effect of soaking is not comparable to injection's.

Figure 19 displays that the smaller the distance of the fracture in the infill well relative to the existing fractures of the parent wells, the more significant the stress restoration will be affected by the parent well injection; subsequently, the less rotated the hydraulic fracture would develop.

## Field examples and verification

Two field examples in the Mabei oil field are used to verify how the parent well production and injection would influence the infill well performance. One example is the well pad of the M region focused on in the previous discussion, and a second one is from a neighboring area of the M region,

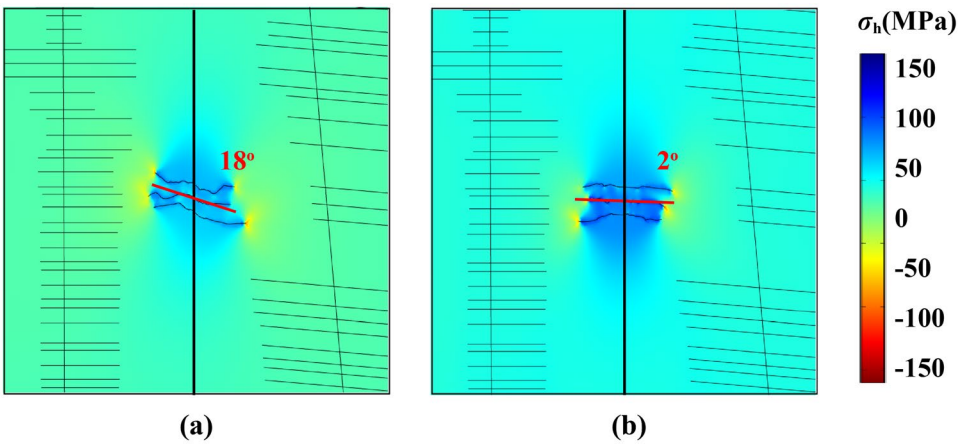


**Fig. 17** Influences of the injection volume on the fracture configuration (the 16th stage of M-I2): **a** $\xi_i = 0.25$, soaking for 0 days; **b** $\xi_i = 0.5$, soaking for 0 days

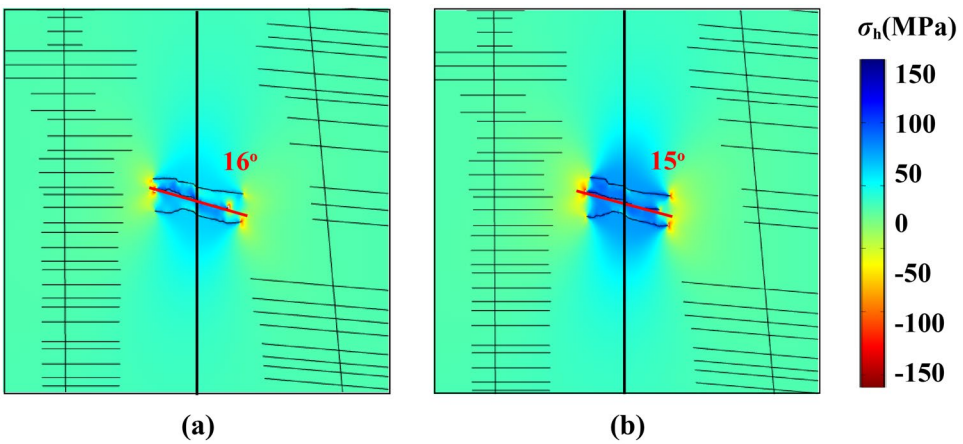


**Fig. 18** Influences of the soaking time on the fracture configuration (the 16th stage of M-I2): **a** $\xi_i = 0.3$, soaking for 0 days; **b** $\xi_i = 0.3$, soaking for 30 days

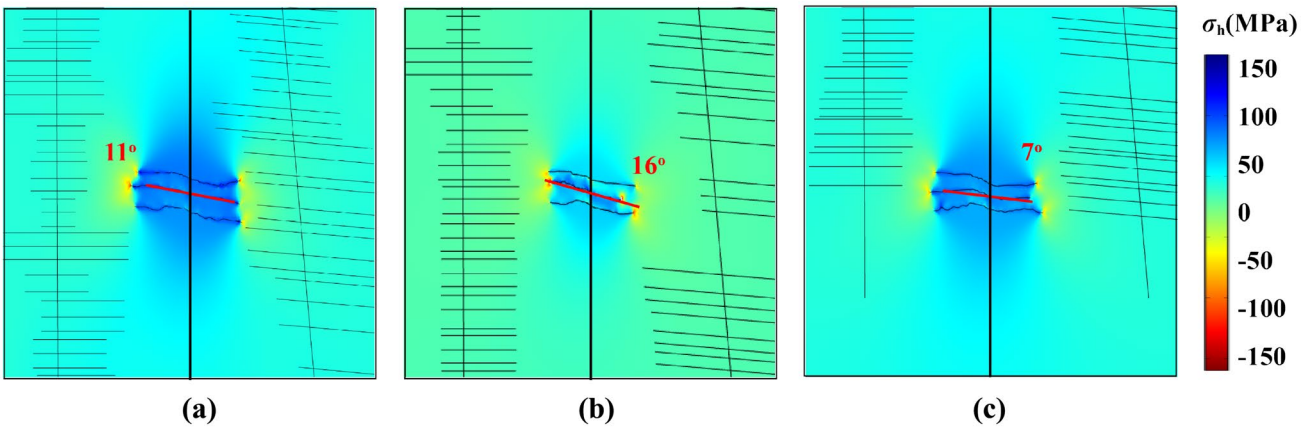


**Fig. 19** Influences of the distance to the parent wells on the fracture configuration of **a** the 7th, **b** 16th and **c** 25th stage

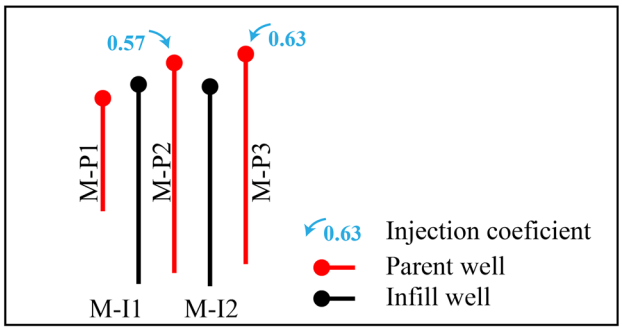


**Fig. 20** Schematic diagram of the three parent wells and the two infill wells in the M region

which has similar stratigraphical lithology and engineering designs. A direct assessment of the fracture morphology is favored to validate the effects of stress evolution on the fracture paths; unfortunately, no microseismic monitoring was undertaken in the infill wells to conduct such an evaluation. Therefore, the production data of the infill wells were used instead for verification purposes.

## Field example one—the M region of the Mabei oil field

The schematic diagram of the three parent wells and the two infill wells of the M region is displayed in Fig. 20. Table 7 shows the production and injection volume of the three parent wells, M-P1, M-P2, and M-P3, having a cumulative liquid production volume of 50,903, 46,655, and 47,532 $m^3$, respectively. Before fracturing the two infill wells, 15,066 and 15,060 $m^3$ of water was injected into wells M-P2 and M-P3 to recharge the formation pressure, whereas no

**Table 7** Well completion, production and injection information of the parent and infill wells (the M region)

(a) Parent well production/injection information

| Parent well | Fracturing fluid volume, $V_f$ ($m^3$) | Liquid production volume, $V_p$ ($m^3$) | Depletion volume, $V_d$ ($m^3$) | Injection volume, $V_i$ ($m^3$) | $V_i/V_d$ (-) |
|---|---|---|---|---|---|
| M-P1 | 6248 | 50,903 | 44,655 | 0 | 0 |
| M-P2 | 20,163 | 46,655 | 26,492 | 15,066 | 0.57 |
| M-P3 | 23,766 | 47,532 | 23,766 | 15,060 | 0.63 |

(b) Infill well production information

| Infill well | Production time, (d) | Oil production volume, $V_p$ (t) | Avg. oil production per day, (t/d) |
|---|---|---|---|
| M-I1 | 148 | 450 | 3.04 |
| M-I2 | 150 | 2230.4 | 14.9 |

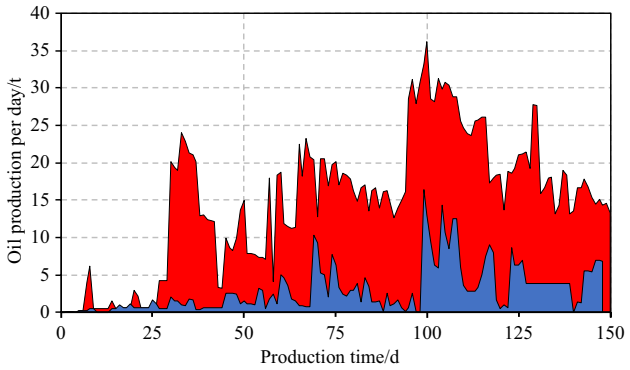


**Fig. 21** Oil production per day of the two infill wells

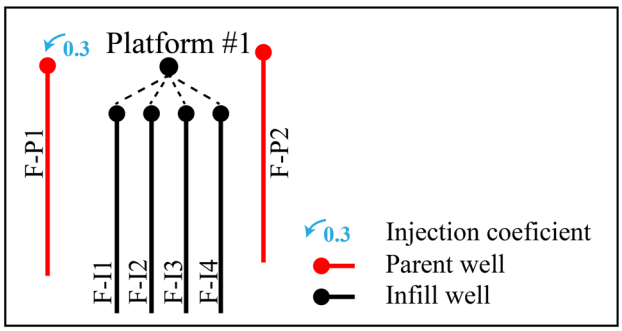


**Fig. 22** Schematic diagram of the two parent wells and the four infill wells in the F region

injection occurred in well M-P1. Figure 21 shows that the production of M-I2 is significantly higher than that of M-I1, which proves that the water injection in the neighboring parent wells does significantly increase the production of the adjacent infill wells.

## Field example two—the F region of the Mabei oil field

To further verify the discoveries of the stress field evolution and the accompanying fracture development, the stimulation history of the F region having two parent and four infill wells (Fig. 22) was chosen as a second field example. F-P1 and F-P2 are the two parent wells, and F-I1 to F-I4 are the four infill wells. The legacy production of F-P1 and F-P2 has resulted in different degrees of pressure depletion in the surrounding formation, as listed in Table 8. Wells F-P1 and F-P2 started production in 2016 with a cumulative liquid production volume of 40,844 and 38,307 $m^3$, respectively. Platform #1 was deployed in 2021. The average horizontal section length is 1200 m, and the well spacing is 200 m. The distance is 350 m between F-P1 and F-I1 and 200 m between F-I4 and F-P2. Before fracturing the four infill wells, 8000 $m^3$ of water was injected into well F-P1, whereas no injection was implemented in well F-P2.

Figure 23 shows the cumulative oil production of the four infill wells after 123 to 143 days. It is worth mentioning that the production data are the only accessible information at the current stage, though the production of a more extended period can be more insightful. The production volumes of wells F-I1 and F-I2 are significantly higher than F-I3 and F-I4, which proves that the water injection in the parent well F-P1 can significantly raise the production of the adjacent infill wells (F-I3 and F-I4). The production of wells F-P1 and F-P2 led to decreased formation pressure and deflected stress orientation. Upon reinjection in well F-P1, the formation pressure was strengthened, and the stress orientation of its neighboring formation area gradually recovered to the original states, producing more extensive and perpendicular fractures relative to the well paths of F-I1 and F-I2 rather than F-I3 and F-I4.

The infill well completion shall be constrained at a level such that the fractures do not penetrate the depleted zone and

**Table 8** Well completion, production, and injection information of the two parent wells (F region)

(a) Well completion information

| Parent well | Horizontal length (m) | Number of stages (−) | Number of clusters (−) | Start date of production (Year/Month) |
|---|---|---|---|---|
| F-P1 | 1208 | 18 | 36 | 2016/08 |
| F-P2 | 1206 | 20 | 39 | 2016/09 |

(b) Production/Injection information

| Parent well | Fracturing fluid volume, $V_f$ ($m^3$) | Liquid production volume, $V_p$ ($m^3$) | Depletion volume, $V_d$ ($m^3$) | Injection volume, $V_i$ ($m^3$) | $V_i/V_d$ (−) |
|---|---|---|---|---|---|
| F-P1 | 14,521 | 40,844 | 26,323 | 8000 | 0.30 |
| F-P2 | 17,456 | 38,307 | 20,851 | 0 | – |

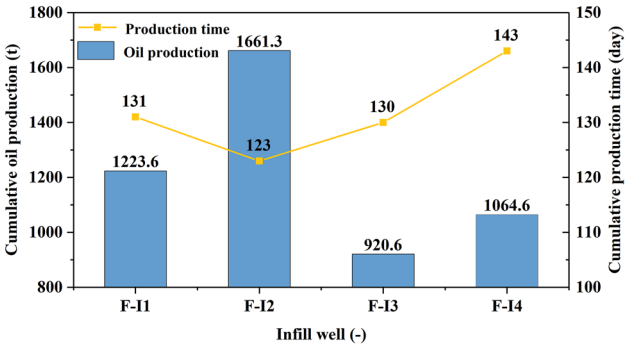


**Fig. 23** Cumulative oil production of the four infill wells (F region)

communicate with the fracture network of the parent wells. In this respect, additional field test methods, especially microseismic recording, shall be carried out to explicitly disclose the fracture extension, which will become another exciting topic of research in the future.

## Conclusions

Various production and injection schemes can sharply affect the stress field and the fracture propagation in a horizontal well pad that contains both parent and infill wells. This study proposed a customized finite element approach to quantitatively evaluate the stress evolution of multiple wells distributed with complex planar fractures and predict the irregular hydraulic fracture propagation. Several conclusions can be drawn as follows.

(1) The legacy production has dramatically altered the formation pressure and stress field in the parent wells' area. Such changes inevitably result in negative inter-well interference for the infill wells if no injection practice is conducted.
(2) The hydraulic fractures in an infill well will be constrained in the low-pressure region, and their paths deviate from the normal directions relative to the horizontal well path. Reinjection in the parent wells can partially restore the formation pressure and stress magnitudes and their orientations, leading to more transversely developed fractures, larger SRV of the infill well, and ultimately greater production capacity.
(3) The injection plays a much more significant role in restoring the pressure and stress field than the soaking of the parent wells.
(4) As the injection volume increases, the extent of such a restoration strengthens, causing minor deviation of the hydraulic fractures in the infill well.
(5) As the distance between the hydraulic fractures of the infill well and the existing fractures of the parent wells decreases, the orientation of the former set of fractures will be more strongly affected by the injection of the parent wells.

Future research will be dedicated to identifying the boundary distance between the positive and negative inter-well interferences. The optimum amount of injection for a specific parent well is also desired when weighing the infill well's expected productivity, time management, and financial investment. Finally, the microseismic events recorded in an infill well rather than the production data can reveal more obvious evidence of its fracture development after implementing a particular injection design in the parent wells.

**Acknowledgements** This research was funded by the National Natural Science Foundation of China (No. 42277122), the Research Found of China University of Petroleum, Beijing (No. 2462020YXZZ030). Gratitude is also attributed to the Xinjiang Oilfield Corporation for providing us the in situ cores and the field data.

**Author contribution** The submission has been received explicitly from all co-authors. And authors whose names appear on the submission have contributed sufficiently to the scientific work and therefore share collective responsibility and accountability for the results.

**Funding** The National Natural Science Foundation of China, 42277122, Botao Lin, the Science Foundation of China University of Petroleum, Beijing, 2462020YXZZ030, Botao Lin.

## Declarations

**Conflict of interest** The authors declare no conflict of interest.

**Consent for publication** I certify that this manuscript is original and has not been published and will not be submitted elsewhere for publication while being considered by JPEPT. And the study is not split up into several parts to increase the quantity of submissions and submitted to various journals or one journal over time. No data have been fabricated or manipulated (including images) to support your conclusions. No data, text, or theories by others are presented as if they were our own.

## References


Ajani AA, Kelkar MG (2012) Interference study in shale plays. In: SPE hydraulic fracturing technology conference, the Woodlands, Texas, 6–8 February. https://doi.org/10.2118/176910-MS

Dave R, Mark M, Garrett F (2022) Modelling of parent child well interactions. In: The SPE hydraulic fracturing technology conference & exhibition, Woodlands, Texas, USA, 1–3 February. https://doi.org/10.2118/209152-MS

Dean RH, Gai X, Stone CM et al (2006) A comparison of techniques for coupling porous flow and geomechanics. SPE J 11(1):132–140. https://doi.org/10.2118/79709-PA

Esquivel R, Blasingame TA (2017) Optimizing the development of the Haynesville Shale—lessons learned from well-to-well hydraulic fracture interference. In: Unconventional resources technology conference, Austin, Texas, 24–26 July. https://doi.org/10.15530/URTEC-2017-2670079

Fiallos MX, Yu W, Ganjdanesh R et al (2019) Modeling interwell interference due to Complex fracture hits in eagle ford using EDFM. In: International petroleum technology conference, Beijing, China, 26–28 March. https://doi.org/10.2523/IPTC-19468-MS.

Fisher MK, Wright CA, Davidson BM et al (2005) Integrating fracture mapping technologies to improve stimulations in the Barnett shale. SPE Prod Facil 20:285–293. https://doi.org/10.2118/77441-PA

Fisvhler MA, Bolles RC (1981) Random sample consensus: a paradigm for model fitting with applications to image analysis and automated cartography. Commun ACM 24:6381–6395. https://doi.org/10.1016/B978-0-08-051581-6.50070-2

Gai X, Dean RH, Wheeler MF et al (2003) Coupled geomechanical and reservoir modeling on parallel computers. In: SPE reservoir simulation symposium, Houston, 3–5 February. https://doi.org/10.2118/79700-MS

Gakhar K, Rodionov Y, Defeu C, Shan D, Malpani R, Ejofodomi E, Fischer K, Hardy B (2017) Engineering an effective completion and stimulation strategy for infill wells. In: SPE hydraulic fracturing technology conference and exhibition, the Woodlands, Texas, USA, Jan 24–26. https://doi.org/10.2118/184835-MS

Gao JJ, Lau HC, Sun J (2020) A semianalytical poroelastic solution to evaluate the stability of a borehole drilled through a porous medium saturated with two immiscible fluids. SPE J 25(05):2319–2340. https://doi.org/10.2118/195515-PA

Geertsma J, de Klerk F (1969) A rapid method of predicting width and extent of hydraulically induced fractures. J Pet Technol 21:1571–1581. https://doi.org/10.2118/2458-PA

Guo X, Wu K, Killough J, Tang J (2019a) Understanding the mechanism of interwell fracturing interference with reservoir/geomechanics/fracturing modeling in eagle ford shale. SPE Reserv Eval Eng 22:842–860. https://doi.org/10.2118/194493-PA

Guo X, Wu K, An C, Tang J, Killough J (2019b) Numerical investigation of effects of subsequent parent-well injection on interwell fracturing interference using reservoir-geomechanics-fracturing modeling. SPE J 24:1884–1902. https://doi.org/10.2118/195580-PA

Gupta J, Zielonka M, Albert RA et al (2012) Integrated methodology for optimizing development of unconventional gas resources. In: SPE hydraulic fracturing technology conference, the Woodlands, Texas, 6–8 February. https://doi.org/10.2118/152224-MS

Gupta I, Rai C et al (2020a) A data-driven approach to detect and quantify the impact of frac-hits on parent and child wells in unconventional formations. In: SPE/AAPG/SEG unconventional resources technology conference, virtual, 20–22 July. https://doi.org/10.15530/urtec-2020-2190

Gupta I, Rai C, Devegowda D et al (2020) Haynesville shale: predicting long-term production and residual analysis to identify well interference and fracture hits. SPE Reserv Eval Eng 23(01):132–142. https://doi.org/10.2118/195673-PA

He Y, Guo J, Tang Y et al (2015) Interwell fracturing interference evaluation of multi-well pads in shale gas reservoirs: a case study in WY basin. In: SPE annual technical conference & exhibition, Denver, Colorado, USA, 5–7 October. https://doi.org/10.2118/201694-MS

Hidayati DT, Chen HY, Teufel LW (2001) Flow-induced stress reorientation in a multiple-well reservoir. In: SPE rocky mountain petroleum technology conference, Keystone, Colorado, May 21–23. https://doi.org/10.2118/0801-0056-JPT

Kurtoglu B. Salman A (2015) How to utilize hydraulic fracture interference to improve unconventional development. In: Abu Dhabi international petroleum exhibition and conference, Abu Dhabi, UAE, Nov 9–12. https://doi.org/10.2118/177953-MS

Li SY, He TM, Yin XC et al (2010) Introduction of Rock Fracture Mechanics. Press of University of Science and Technology of China, Hefei, China

Li JM, Wu BC, Zhao HY, Cheng N, Huang JL (2019) Adaptability of horizontal well volume fracturing to tight conglomerate reservoirs in Mahu oilfield. China Pet Explor 24(2):250–259

Li WX, Song L, Xi CM, Xie SY, Rong KS (2021) Drilling and completion technology for horizontal well with ultra-long horizontal section in tight conglomerate reservoir of xinjiang Mahu oilfield. Xinjiang Oil Gas 17(04):86–91

Lindsay G, Miller G, Xu T et al (2018) Production performance of infill horizontal wells vs. pre-existing wells in the major US unconventional basins. In: SPE hydraulic fracturing technology conference and exhibition, the Woodlands, Texas, 23–25 January. SPE-189875-MS. https://doi.org/10.2118/189875-MS

Liu X, Jin Y, Lin B et al (2018) An enhanced RANSAC method for complex hydraulic network characterization based on microseismic data. In: The 2nd international discrete fracture network engineering conference, June 20–22. ARMA-DFNE-18–0575

Marongiu-Porcu M, Lee D, Shan D et al (2016) Advanced modeling of interwell-fracturing interference: an eagle ford shale-oil study. SPE J 21(5):1567–1582. https://doi.org/10.2118/174902-PA

Maxwell SC, Rutledge J, Jones R et al (2010) Petroleum reservoir characterization using downhole microseismic monitoring. Geophysics 75:5129–5137. https://doi.org/10.1190/1.3477966

Miller G, Lindsay G, Baihly J et al (2016) Parent well refracturing: economic safety nets in an uneconomic market. In: SPE low perm symposium, Denver, Colorado, 5–6 May. SPE-180200-MS. https://doi.org/10.2118/180200-MS

Mukherjee H, Poe B, Heidt H, Watson T, Barree RD (1995) Effect of pressure depletion on fracture geometry evolution on fracture geometry evolution and production performance. In: SPE annual technical conference and exhibition, Dallas, Texas, USA, Oct 22–25. SPE 30481. https://doi.org/10.2118/65064-PA

Roussel NP, Florez HA, Rodriguez AA (2013). Hydraulic fracture propagation from infill horizontal wells. In: SPE annual technical conference and exhibition, New Orleans, USA, Sep 30-Oct 2, SPE 166503

Safari R, Lewis R, Ma X et al (2017) Infill-well fracturing optimization in tightly spaced horizontal wells. SPE J 22(2):582–595. https://doi.org/10.2118/178513-PA

Settari A, Mourits FM (1998) Coupled Reservoir and geomechanical simulation system. SPE Journal. 3(3):219–226. https://doi.org/10.2118/50939-PA

Shi C, Lin B, Yu H et al (2022) Characterization of hydraulic fracture configuration based on complex in situ stress field of a tight oil reservoir in Junggar Basin. Acta Geotechnica, Northwest China. https://doi.org/10.1007/s11440-022-01607-4

Sih GC (1974) Strain-energy-density factor applied to mixed mode crack problems. Int J Fract 10(3):305–321. https://doi.org/10.1016/0148-9062(74)92039-7

Wei SM, Chen M, Jin Y, Lu YH, Liu X, Wen H (2018) Numerical simulation of dynamic stress field of fractured horizontal well in carbonate reservoirs-in the production process. In: 2nd international discrete fracture network engineering conference, 2018

Wei SM, Kao JW, Jin Y, Shi C, Xia Y, Liu S (2021) A discontinuous discrete fracture model for coupled flow and geomechanics based on FEM. J Pet Sci Eng 204:108677. https://doi.org/10.1016/j.petrol.2021.108677

Xu JW, Li JM, Wu YY, Ding K, Jiang H (2019) Exploration and practice of volume fracturing technology in horizontal well of Mahu tight conglomerate reservoirs. China Pet Explor 24(2):241–249

Yang X, Yu W, Wu K et al (2020) Assessment of production interference level due to fracture hits using diagnostic charts. SPE J Preprint. https://doi.org/10.2118/200485-PA

Zhang JY, Teng XL, Qiu L, Zhu WM (2011) Case study on wells interference and technical measures in infill well fracturing. Pet Geol Eng 25(1):95–97

Zoback MD (2010) Reservoir Geomechanics. Cambridge University Press, UK, p 449

Zou LZ, Zou LX, Jiang XM, Liu YB, Lu ZY, Li WX (2018) The horizontal drilling technology in tight sandy conglomerate reservoirs in Mahu sag. Xinjiang Oil Gas 14(03):19–24